Energy & Environmental Science

ROYAL SOCIETY OF CHEMISTRY

PAPER

View Article Online
View Journal | View Issue

Cite this: *Energy Environ. Sci.*, 2024, **17**, 5993

Optimizing interface concentration and electric fields for enhanced lithium deposition behavior in lithium metal anodes†

Jiaxiang Liu,[a] Haiming Hua,[b] Jie Lin,[e] Yongliang Deng,[b] Nanbiao Pei,[b] Peng Zhang,*[ac] Jin-Chao Dong,*[ac] Jian-Feng Li *[abc] and Jinbao Zhao *[abcd]

Understanding dynamic fluctuations in complex multi-physics fields at an electrolyte/electrode interface is crucial for explaining the lithium deposition mechanism and developing efficient interface structures, but there are significant challenges. Here, we introduce an internal standard substance (1,1,2,2-tetrafluoroethyl-2,2,3,3-tetrafluoropropyl ether (TTE)) to propose a quantitative *in situ* Raman spectroscopy method to disclose the variation of interfacial concentration field. It is proved that the formation of an anion depletion layer at the electrolyte/electrode interface during lithium deposition leads to the formation of a space charge layer (SCL) with local electric field, which can accelerate dendrite growth and is closely related to the withdrawal of anions from interface. Further, a high-anion-concentration interface (HACI) with immobilized anions is proposed. This HACI can effectively prevent anion depletion at the interface and enhance the interfacial Li^+ transference number from 0.30 to 0.57, thus alleviating formation of SCL and facilitating uniform lithium deposition. Hence, a full cell with high-load NCM523 cathode (~14 mg cm^{-2}) and limited HACI@Li anode (~50 μm) delivers excellent cycling over 200 cycles with a high discharge capacity retention of 77.6% (~125.7 mA h g^{-1}). This offers critical insights for designing lithium battery systems from the perspective of multi-physics fields.

Received 25th April 2024,
Accepted 28th June 2024

DOI: 10.1039/d4ee01816h

rsc.li/ees

Broader context

Lithium metal batteries show great potential for next-generation energy storge systems due to the extremely high energy density of the lithium metal anode. However, its uncontrollable deposition behaviour and complicated interfacial processes will result in dendrite growth and unstable interphase, restraining its application. The exploration of complex interfacial processes is significant for comprehension of the chemical process for the lithium metal anode, which can further direct the modification strategies. Herein, we employed quantitative *in situ* electrochemical enhanced Raman spectroscopy and finite element analysis to examine the concentration and electrical field at the electrolyte/electrode interface. We first obtained direct fingerprint spectral evidence of the formation and quantitative evolution process of an anion depletion layer, indicating the formation of a space charge layer with uneven electrical field. Further, the core factors affecting the generation of the space charge layer are revealed and a novel high-anion-concentration interface utilizing an anion immobilization strategy is proposed. It can effectively mitigate the anion depletion and space charge effect, thus facilitating the uniform deposition of lithium. This indicates that the optimization of multi-physical fields *via* interface architecture is an effective method to promote the uniform deposition of lithium and desirable long-term cycling performance.

[a] *College of Energy, Xiamen University, Xiamen 361102, P. R. China. E-mail: pengzhang@xmu.edu.cn, jcdong@xmu.edu.cn, Li@xmu.edu.cn, jbzhao@xmu.edu.cn*
[b] *College of Chemistry and Chemical Engineering, Xiamen University, Xiamen 361005, P. R. China*
[c] *Tan Kah Kee Innovation Laboratory (IKKEM), Xiamen 361005, China*
[d] *State-Province Joint Engineering Laboratory of Power Source Technology for New Energy Vehicle, State Key Laboratory of Physical Chemistry of Solid Surfaces, Engineering Research Center of Electrochemical Technology, Ministry of Education, Collaborative Innovation Center of Chemistry for Energy Materials, Xiamen University, Xiamen, 361005, P. R. China*
[e] *School of Mechanical and Aerospace Engineering, Queen's University Belfast Ashby Building, Stranmillis Road, Belfast BT9 5AH, UK*

† Electronic supplementary information (ESI) available. See DOI: https://doi.org/10.1039/d4ee01816h

Introduction

The pursuit of environmentally friendly society motivates the booming development of a greener chemical industry, shifting from fossil fuels as energy sources to renewable energy. Therein, an energy storage system (such as batteries) acts as a critical buffering method for the seasonal fluctuation of renewable energy supply. However, lithium-ion batteries, the most common energy storage application, are restricted because of limited energy density.[1] This arouses an enthusiasm for exploiting high-energy cathodes (such as sulfur and O_2) and anodes

(such as silicon and metal).[2,3] Li metal anode is known as the "holy grail" of anodes for its ultrahigh theoretical specific capacity (3860 mA h g^{-1}) and extremely low standard redox potential (−3.04 V *vs.* standard hydrogen electrode, SHE).[4,5] However, its practical applications are hindered by its primitive the uncontrollable electrodeposition behavior, growth of dendrites and fragile solid–electrolyte interphase (SEI).[6,7] Consequently, Li metal batteries suffer from low Coulombic efficiency (CE), short cycle life and severe safety issues. To address these concerns, comprehensive strategies, including substrate design,[3,8] SEI engineering[9–11] and electrolyte optimization,[12–14] have been proposed.

Traditional SEI engineering mainly focuses on regulating Li^+ flux and inhibiting parasitic reactions between electrolyte and lithium anode.[15–18] Therein, much attention is attached to the interphase, rather than the interface,[19] while the intricate multi-physics fields at the electrolyte/electrode interface are usually neglected. During lithium deposition, the multi-physics fields at the narrow interface, including concentration field, electric field, temperature field and stress field, will undergo dramatic fluctuation and significantly affect the lithium deposition behavior.[20] Resolving the dynamic variation of these intricate multi-physics fields, as well as their impact on the deposition process of lithium, is imperative to the further comprehension of lithium deposition behaviors.

Different from the temperature field and stress field which are often optimized *via* external regulation,[21–23] the concentration field and electric field describe the intrinsic induction and growth process of lithium. According to Sand's time model,[24–26] a limited Li^+ diffusion rate could lead to a Li^+ concentration gradient, which may trigger self-amplified dendrite growth. Further, the space-charge model[27,28] describes the locally aggregated electric field of the space charge layer (SCL) caused by anion depletion at the electrolyte/electrode interface. The model description and experimental evidence of the SCL have been proposed for traditional Cu and Zn deposition in aqueous electrolytes.[29–31] It manifests that the formation of the SCL could induce a potential drop near the electrode (up to 3 V)[31] and results in ramified lithium growth, whose speed is governed by the speed at which anions withdraw from the interface.[32,33] Many researchers have also proposed strategies to mitigate SCL formation for lithium metal anodes.[34,35] However, restricted by the sensitivity of the lithium anode to H_2O and atmosphere, an accurate description of the interfacial ionic concentration field and electric field for non-aqueous lithium metal anode, as well as the evolution of the space charge effect, is still not available.

In this study, *in situ* Raman spectroscopy is applied to track the evolution of the interfacial concentration field. Combining with finite element analysis (FEA) and molecular dynamics (MD) simulation, the evolution of the anion depletion layer and electric field at the electrolyte/electrode interface is captured, indicating the formation of SCL. The intense electric field at the SCL will induce fast growth of lithium dendrites, whose magnitude is highly associated with anion species, solvation structure and solvent environment. Therein, the anion transport behavior is the core factor, which can be indirectly described by the cation transference number (t_+).

Further, a high-anion-concentration interface (HACI) is proposed to optimize the concentration and electric fields at the electrolyte/electrode interface (Fig. 1(a)). It immobilizes a high concentration of anions at the interface to inhibit anion depletion and effectively enhance the interfacial t_+ from 0.30 to 0.57, thus preventing the formation of SCL. Hence, the HACI facilitates uniform lithium deposition without dendrites and suppresses parasitic reactions. The full cell test with a high-load NCM523 cathode (∼14 mg cm^{-2}) and a limited lithium anode (∼10 mA h cm^{-2}) modified by HACI shows desirable cycle performance, maintaining a high discharge capacity retention of 77.6% (∼125.7 mA h g^{-1}) after 200 cycles. This multi-physics field regulation provides us an innovative perspective of metal deposition behavior.

Results and discussion

Electrochemical behavior of lithium deposition

The electrochemical behavior of a lithium metal anode is profoundly influenced by the fluctuation of multi-physics fields at the electrolyte/electrode interface. Here, the galvanostatic polarization curve (Fig. S1, ESI†) presents a typical potential drop region at the initial stage of Li deposition (Fig. 1(b)). The deposition substrate is lithium metal to eliminate the nucleation overpotential caused by heterogeneous nucleation.[36,37] Hence, the initial overpotential ($\Delta\eta$) can be mainly ascribed to the interfacial multi-physics field deviation.[38]

To further reveal the source of the potential drop, three kinds of electrolytes with different anion species and solvent environment are probed: (1) EC/DEC-1 M-$LiPF_6$; (2) EC/DEC-1 M-LiTFSI; (3) DOL/DME-1 M-LiTFSI (details are in Method). Fig. 1(c) shows that EC/DEC-1 M-$LiPF_6$ exhibits the highest $\Delta\eta$ of 93.6 mV. In contrast, $\Delta\eta$ obviously decreases to 32 mV when PF_6^- anion is replaced by $TFSI^-$. Notably, when the solvent environment is further altered to DOL/DME, a negligible $\Delta\eta$ is observed. It is shown that $\Delta\eta$ is highly related to anion species and solvent environment, which could correspond to the potential drop caused by the local electric field of SCL.[30] Further investigation into the relationship between $\Delta\eta$ and increasing current density (Fig. 1(d) and Fig. S2, ESI†) reveals that $\Delta\eta$ will gradually increase with a boost of applied current density. The increase of $\Delta\eta$ is approximately proportional to the square root of current density, which is in good agreement with the space charge model, as expressed below (eqn (1)).[28] This further demonstrates that $\Delta\eta$ is highly associated with the formation of SCL.

$$-x_I J = \left\{\frac{3[V(L) - V(0)]}{2}\right\}^2 \varepsilon\varepsilon_0 t_+/2 \quad (1)$$

where x_I is a point at the interface; J is the electric current density through the system; V is the electrostatic potential varying from $V(0)$ at $x = 0$ to about $V(L)$ at $x = x_I$; ε_0 is vacuum permittivity; and ε is the dielectric constant of the electrolyte.

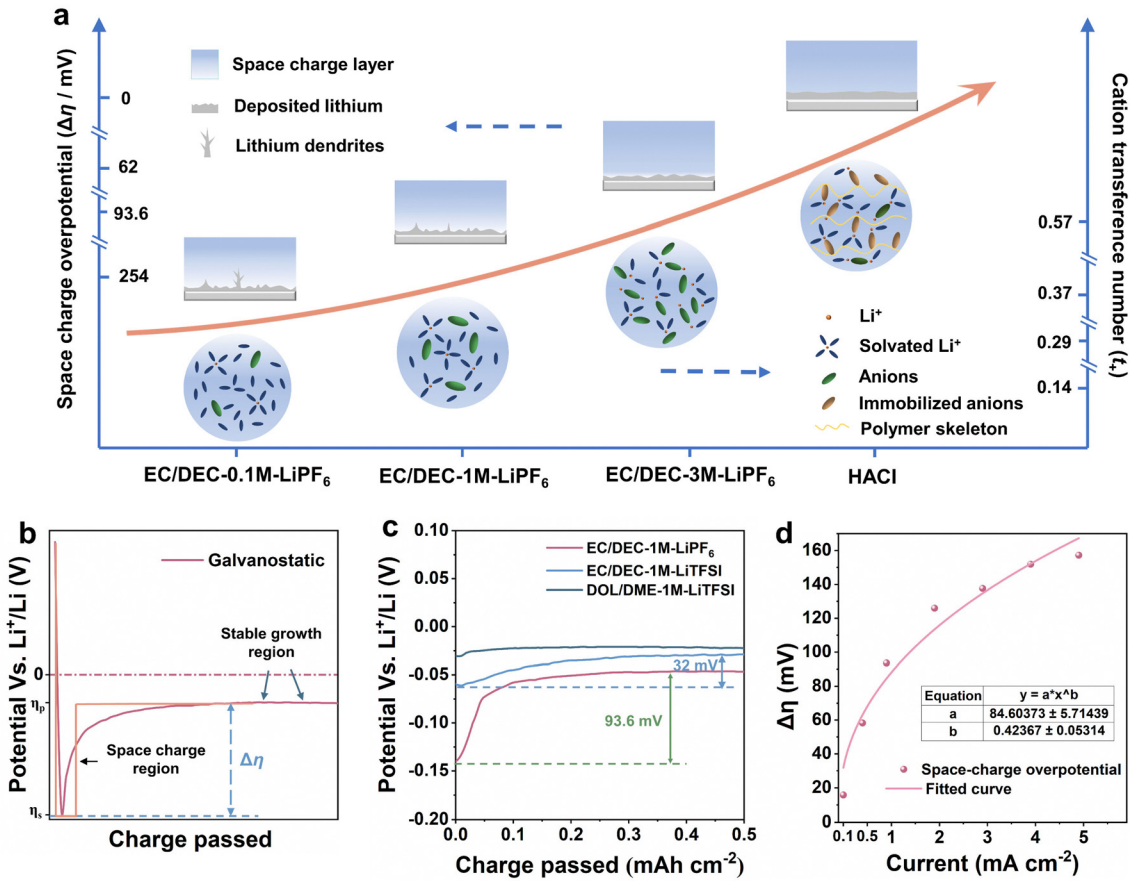

Fig. 1 (a) Schematic illustration of interfacial solvated structure and cation transference number of HACl and electrolytes with different concentration, as well as their effect on the magnitude of SCL and lithium deposition morphology. (b) Schematic plot of the typical potential profiles of galvanostatic lithium deposition on lithium substrate. (c) Potential profiles of galvanostatic lithium deposition on lithium substrate in different electrolytes and corresponding potential drop. (d) Variation of potential drop during galvanostatic lithium deposition at different current densities in EC/DEC-1 M-$LiPF_6$ electrolyte.

The formation of SCL is mainly imputed to the anion depletion near the electrode. Hence, revealing the migration and distribution of anions is vital to evaluate and retard the formation of SCL for a lithium metal anode. However, the fluctuation of multi-physics fields is always restricted within a narrow distance near the electrode surface (~30 Å), hampering accurate measurement.

In situ Raman spectroscopy of interfacial concentration field

Surface-enhanced Raman spectroscopy (SERS) is a fingerprint spectroscopy technique with single-molecule detection sensitivity, which can effectively yield information of electrode surface interface and active chemical species in the sub-nanometer range, and is widely used in molecular structure, solvent structure, electrolyte interaction and other fields.[39–42] In the current work, we employ a methodology involving the establishment of laser pathways to meticulously investigate the reaction kinetics occurring at the electrolyte/electrode interface through *in situ* Raman spectroscopy (Fig. 2(a) and Fig. S3, ESI†). Additionally, within this system, the Cu electrode interface functions as a metal substrate endowed with a potent capability to enhance Raman signals. Consequently, this capability enables us to efficiently acquire enhanced Raman spectroscopic insights into surface/interface species (Fig. 2(b)).

As shown in Fig. 2(c), *in situ* Raman measurement is conducted with three typical electrolytes (EC/DEC-1 M-$LiPF_6$, EC/DEC-1 M-LiTFSI and DOL/DME-1 M-LiTFSI) and three characteristic signals in Raman spectroscopy are focused on: anions, coordinated solvents and free solvents (Fig. 2(c)). From the point of view of quantitative analysis, under identical positional and potential conditions, the variation in Raman peak intensity of characteristic species on the electrode surface exhibits a strong correspondence with their concentration or coverage. Consequently, in our investigation, we can simply correlate changes in Raman peak intensity with changes in concentration. Fig. 2(d) presents the interfacial variation of different species in EC/DEC-1 M-$LiPF_6$, when cathodic galvanostatic polarization is applied. Two typical processes are observed at the interface. (1) The Raman peak intensity of coordinated EC molecules (~910 cm^{-1}) decreases while that of free EC molecules (~890 cm^{-1}) increases,[43] implying the desolvation of solvated Li^+ preceding its reduction to metallic Li. (2) The Raman peak intensity of PF_6^- (~741 cm^{-1})[44] rapidly drops, suggesting that PF_6^- is rapidly repulsed from the interface and

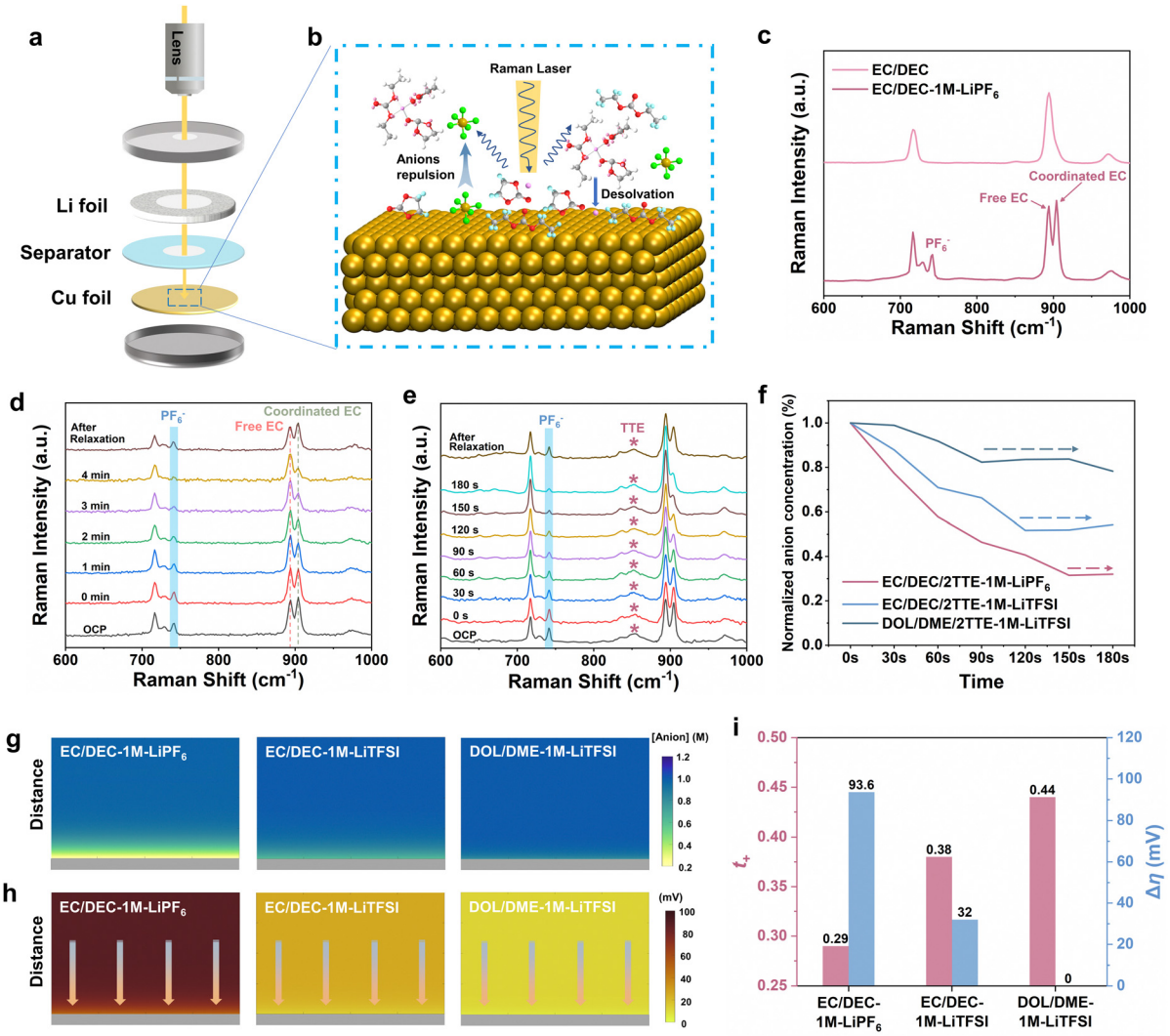

Fig. 2 (a) Schematic illustration of the inner structure of simulated coin cell for *in situ* Raman spectroscopy. (b) Principle of Raman scattering for monitoring the interfacial species on the surface of Cu substrate. (c) Raman spectra of EC/DEC-1 M-$LiPF_6$ and pure solvents. (d) Interfacial *in situ* Raman spectra of EC/DEC-1 M-$LiPF_6$ at a current density of 0.1 mA cm^{-2}. (e) Interfacial *in situ* Raman spectra of EC/DEC/2TTE-1 M-$LiPF_6$ at a current density of 0.1 mA cm^{-2}. (f) Variation of the concentration of anions at the interface in different electrolytes at a current density of 0.1 mA cm^{-2}. FEA simulation of the anion concentration field (g) and electric field (h) at the electrolyte/electrode interface in different electrolytes. (i) Cationic transference number and initial potential drop of different electrolytes.

an anion depletion layer is formed. After relaxing for two minutes, interfacial anion depletion recovers *via* diffusion, manifesting that it is a polarization process. The *in situ* Raman spectra also reveal the varying degrees of anion depletion at the electrolyte/electrode interface in different electrolytes (Fig. S4–S6, ESI†).

Considering the complex solvation structure of ions in the electrolyte, in order to enhance the accuracy of quantitative analysis, we introduced 1,1,2,2-tetrafluoroethyl-2,2,3,3-tetrafluoropropyl ether (TTE) as an internal standard substance for quantitative *in situ* Raman spectroscopic analysis in the electrolyte. TTE is an inert diluent extensively applied in localized high-concentration electrolytes, which neither affects the original solvated structure of the electrolyte nor coordinates with Li^+; thus its migration under electric field is negligible.[45,46] Fig. S7 (ESI†) manifests that the addition of TTE will not influence the electrochemical performance and formation of SCL. The broad characteristic peak at around 852 cm^{-1} can be assigned to TTE[47] (Fig. S8, ESI†). Through normalizing the *in situ* Raman spectra during lithium deposition based on the consistent peak of TTE, a quantitative description of various species at the interface is obtained (Fig. 2(e), (f) and Fig. S9, ESI†). As shown in Fig. 2(f), the normalized Raman peak (~741 cm^{-1}) intensity or the concentration of PF_6^- rapidly decreases to near 32% at the interface and a considerable anion depletion layer is formed in EC/DEC/2TTE-1 M-$LiPF_6$. When PF_6^- is replaced by $TFSI^-$, the concentration of $TFSI^-$ decreases to about 52% at the initial 120 s and remains stable later, indicating that anion depletion is mitigated. In contrast, $TFSI^-$ can maintain a high concentration of about 84% at the interface with slight anion

depletion in DOL/DME/2TTE-1 M-LiTFSI electrolyte. Through this method, the formation of anion depletion layer and SCL at the interface during lithium deposition can be disclosed. FEA is also applied to predict the formation of concentration field and concomitant electric field at the electrolyte/electrode interface (Fig. 2(g), (h) and Fig. S10, ESI†). Here, the electric double layer is appended in the interfacial system, which is proved to be significant for the formation of SCL (details in Method). It manifests that EC/DEC-1 M-$LiPF_6$ exhibits a very large anion concentration field, which will result in uneven electric field and potential drop at the electrolyte/electrode interface, in agreement with the *in situ* Raman analysis. This manifests that the formation of an anion depletion layer will continue to SCL with interfacial electric field and potential drop. This is consistent with $\Delta\eta$ in different electrolytes. This shows that $\Delta\eta$ during lithium deposition on lithium substrate can act as a representative parameter to describe the magnitude of SCL. The suppression of anion concentration field can effectively alleviate the uneven interfacial electric field and potential drop near the Li metal anode.

The quantitative Raman analysis is also an effective way to reveal the interfacial concentration field of different species, which can be extended to various electrolyte systems and interfacial processes.

Exploration of SCL

The magnitude of SCL is highly related to anion species, solvated structure, and solvent environment. However, what are the core factors influencing the formation of SCL? Here, two typical parameters describing ion migration in an electrolyte, ionic conductivity and t_+, were measured (Fig. S11 and Table S1, ESI†). The anion transport behavior can be reflected by t_+ in a single-salt electrolyte because the ion transport in the electrolyte is entirely undertaken by Li^+ and anions. An improvement of t_+ indicates the depressed transport of anions. Fig. 2(i) shows that the magnitude of $\Delta\eta$ rapidly decreases with the increase of t_+ for different electrolytes, indicating the reduction of space charge effect. This also conforms to the concentration variation of anions at the electrolyte/electrode interface obtained by *in situ* Raman spectroscopy. MD simulation (Fig. S12–S15, ESI†) also evidences that the severe SCL can be mainly ascribed to the unbalanced and fast migration of anions. The rapid Li^+ transport and suppressed anion migration, indicated by the improvement of t_+, will effectively restrain evolution of anion depletion layer and SCL at the electrolyte/electrode interface.

The formation of SCL will accelerate tip growth of lithium and result in lithium dendrites. EC/DEC-1 M-$LiPF_6$ with very large SCL displays a mossy lithium deposition and inhomogeneous local agglomeration under high current density (Fig. S16a, ESI†). In contrast, more smooth and dense morphology is observed with the mitigation of SCL (Fig. S16b and c, ESI†). The rate performance (Fig. S17, ESI†) and cycle performance (Fig. S18, ESI†) further prove that the electrolytes with weaker SCL will exhibit better cycling performance under high current density. This testifies that the formation of SCL at the electrolyte/electrode interface will dramatically affect the deposition behavior of lithium, inducing tip growth and dendrite generation.

Construction of high-anion-concentration interface

The solvation structure of anions and cations in electrolytes is highly related to salt concentration.[48] An increase of salt concentration can effectively increase t_+ of electrolytes (Fig. S19, ESI†) due to more anion-containing solvation structure,[49,50] thus alleviating the formation of SCL (Fig. S20, ESI†). However, a high-concentration electrolyte will result in high viscosity and low ionic conductivity, restricting its application (Fig. S21, ESI†).

According to the space charge model and results of *in situ* Raman spectroscopy, the formation of SCL mainly extends to a narrow region of the electrolyte/electrode interface. Hence, based on interface regulation, a HACI *via* anion immobilization strategy is proposed to optimize the anion transport behavior and multi-physics fields. It can afford a high-anion-concentration environment at the electrolyte/electrode interface without affecting the bulk electrolyte.

Anions have great implication for the magnitude of SCL and its dissociation is vital to the fast migration of Li^+. Hence, the TVI^- anion with similar structure to $TFSI^-$ is proposed (inset in Fig. 3(a)). It has great compatibility with lithium metal and desirable dissociation capacity which facilitates fast and stable Li^+ transport at the interface. The terminal double bond provides sites for free radical polymerization. Here, an anion-polymer skeleton, in which LiTVI is grafted on flexible polyethylene oxide (PEO) chains (denoted as LiTVI-PEO), is obtained by the γ-ray irradiation grafting method (Fig. S22, ESI†). Traditional ultraviolet and thermal initiation cannot elicit free radicals on PEO chains, thus hindering the grafting reaction. However, the γ-ray irradiation method can facilely initiate free radical grafting on PEO chains and afford homogeneous and pure grafted products, with desirable grafting ratio and fewer impurities (Fig. 3(a)). Fourier transform infrared (FTIR) spectroscopy (Fig. 3(b)), along with ^1H NMR spectra and ^{19}F NMR spectra (Fig. S23, ESI†), manifests the chemical structure of LiTVI and confirms the successful synthesis of LiTVI-PEO. The Raman spectrum (Fig. 3(c)) exhibits an extra peak at around 715 cm^{-1}, which can be assigned to the grafted TVI^- anions.

Furthermore, the polymer skeleton grafted with LiTVI is introduced onto the surface of Li anode by a facile drop-casting method and the most appropriate amount of HACI is studied (Fig. S24–S26, ESI†). Because the variation of anions is mainly restricted within the narrow region at the electrolyte/electrode interface, the artificial HACI should be thin to avoid additional interfacial impedance. In this way, a high concentration of TVI^- ($\sim$2 M) is immobilized at the electrolyte/electrode interface, which can avoid anion depletion to reduce the formation of SCL during lithium deposition. The HACI is uniform and compact with a thickness of around 1.2 μm, tightly adhering to the surface of the lithium anode (Fig. 3(d) and Fig. S27, S28, ESI†). In XPS, two pairs of double peaks in the S 2p spectrum (Fig. 3(e)) can be respectively assigned to

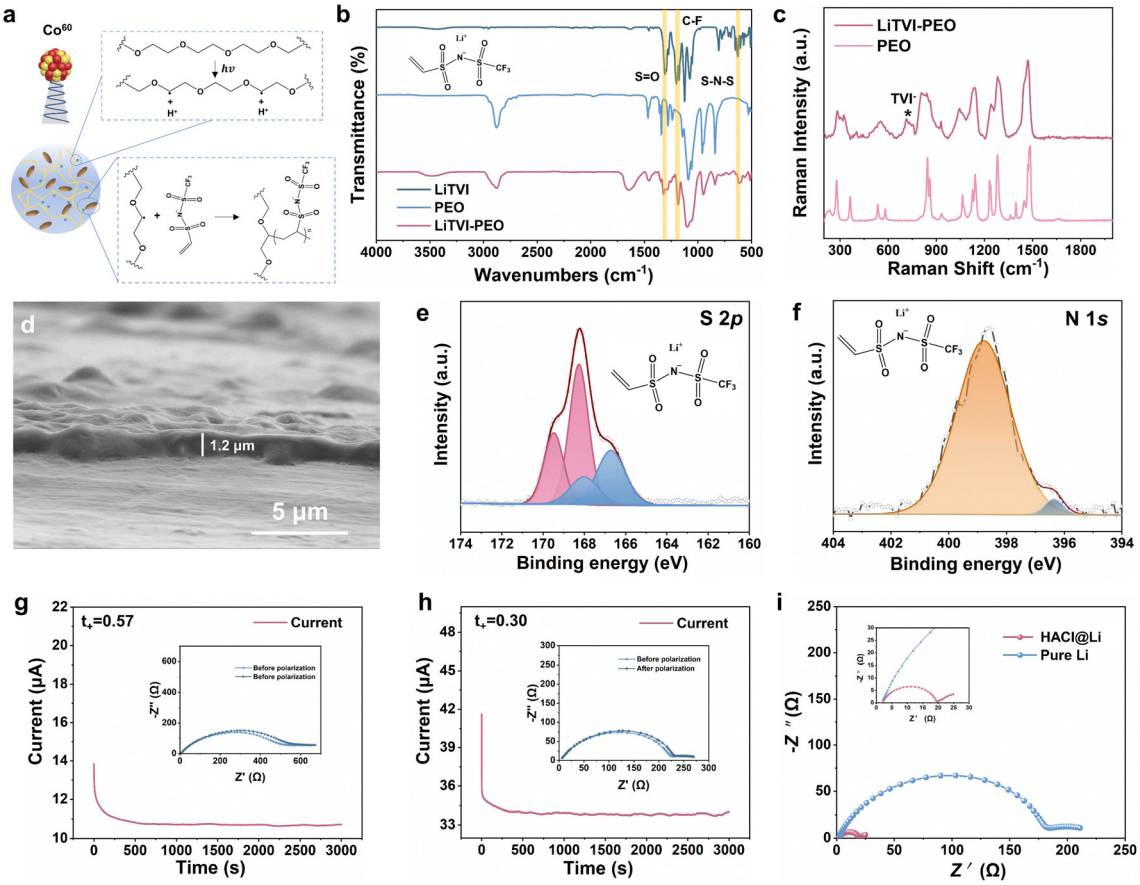

Fig. 3 (a) Schematic illustration of the γ-ray irradiation method for PEO grafting reaction. (b) FTIR spectra of prepared LiTVI salt, pure PEO, and LiTVI-PEO. (c) Raman spectra of pure PEO and LiTVI-PEO. (d) Cross-sectional image of HACl@Li electrode. (e) S 2p spectrum of the HACl@Li electrode. (f) N 1s spectrum of the HACl@Li electrode. Cationic transference number of HACl (g) and EC/DEC-1 M-$LiPF_6$, 10% FEC electrolyte (h) measured by steady-state current method. (i) Electrochemical impedance spectra of HACl@Li electrode and pure Li electrode.

$-SO_2-$ and SO_x and the peak centered at around 399 eV in the N 1s spectrum (Fig. 3(f)) corresponds to the imide group.[51,52] This manifests that TVI^- is successfully immobilized at the surface of the Li anode, forming the HACl. The HACl exhibits a high t_+ of 0.57 (Fig. 3(g)), whereas the t_+ of traditional ester electrolyte is only 0.30 (Fig. 3(h)). Therefore, the HACl can effectively relieve the formation of the anion depletion layer and SCL. The electrochemical impedance spectroscopy (EIS) test (Fig. 3(i)) also reveals that the HACl is a fast Li^+ transport interface, with impedance of only 17.5 Ω. The Tafel curve (Fig. S29, ESI†) also confirms that the HACl exhibits high exchange current density (~0.199 mA cm^{-2}), which is beneficial to reducing the Li^+ concentration gradient and suppressing dendrite growth. The activation energy (E_a) was also determined to study the Li^+ transfer kinetics at the modified interface,[1,53] which reflects the desolvation ability of Li^+. It is shown that the calculated E_a for the HACl@Li electrode is 58.5 kJ mol^{-1}, which is lower than that of pure Li electrode (60.7 kJ mol^{-1}) (Fig. S30 and Table S2, ESI†), proving the effective reduction of the desolvation energy barrier for faster Li^+ transfer. Hence, the HACl can effectively suppress the formation of SCL and accelerate Li^+ transport at the interface to regulate the interfacial concentration and electric fields.

The immobilized anions in the HACl can maintain a high-anion-concentration environment at the electrolyte/electrode interface and restrain the depletion of anions to suppress the formation of SCL, thus facilitating fast and even Li^+ flux (upper in Fig. 4(a)). In contrast, the rapid anion exhaustion at the interface will lead to a notable SCL and cause fast evolution of lithium dendrites (lower in Fig. 4(a)). During lithium deposition, the depletion of anions will result in remarkable electric field, while most anions are immobilized at the HACl, thus restraining the anion depletion and electric field at the electrolyte/electrode interface. Besides, the high concentration of anions at HACl will also gather Li^+ at interface and promote fast Li^+ transfer, thus alleviating the Li^+ concentration gradient caused by Li^+ reduction. In consequence, the even concentration and electric field at HACl will facilitate uniform deposition of lithium. FEA simulation confirms that the anion-immobilized HACl can effectively inhibit the fast evolution of anion concentration field (Fig. S31, ESI†), thus affording an even electric field at the interface (Fig. 4(b)). Further, MD simulation (Fig. 4(c) and Fig. S32, ESI†) also manifests that the HACl can effectively stabilize the Li^+ concentration distribution under electrode potential variation and concentration variation. In contrast, an obvious concentration gradient is

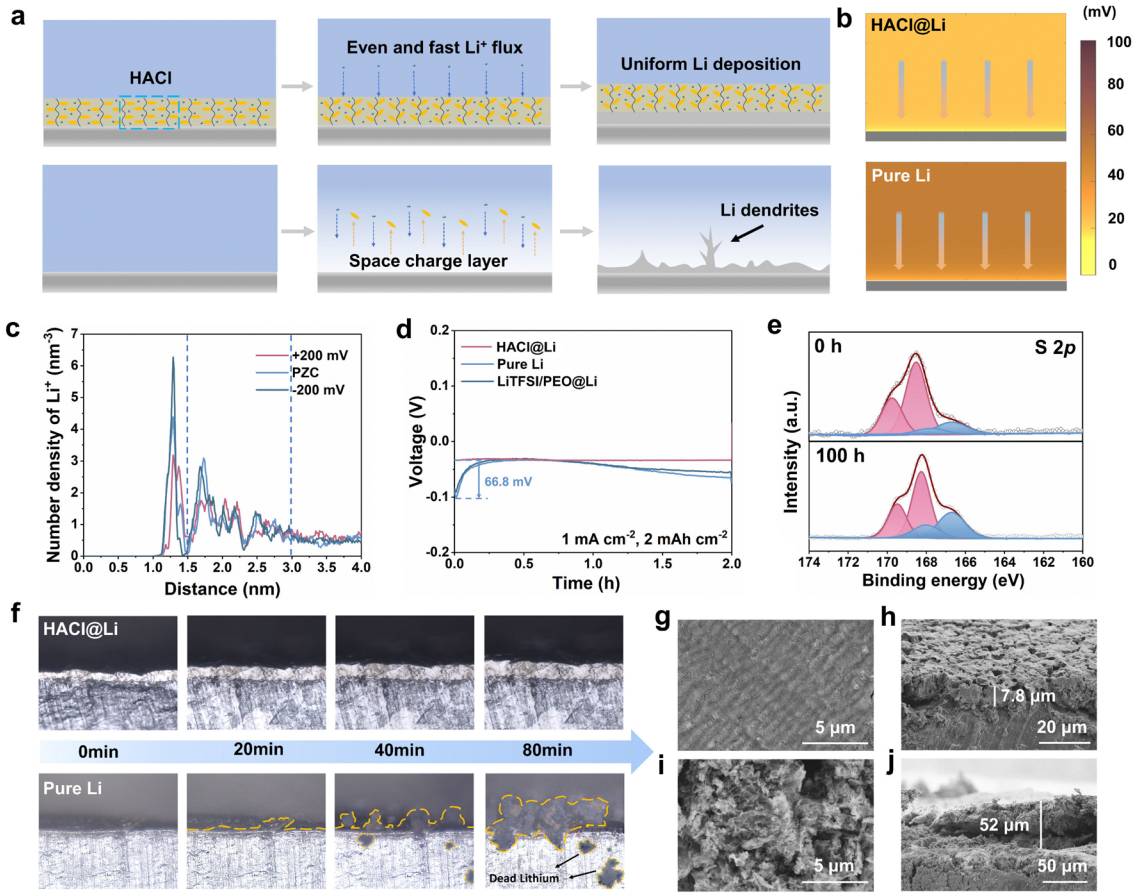

Fig. 4 (a) Schematic illustration of the deposition behavior of HACl@Li electrode and pure Li electrode. (b) FEA simulation of the electric field at the electrolyte/electrode interface with HACl@Li electrode (upper) and pure Li electrode (lower). (c) MD simulation of the variation of Li^+ concentration at HACl under different electrode potentials. (d) Galvanostatic polarization profiles of HACl@Li electrode, pure Li electrode and LiTFSI/PEO@Li electrode. (e) S 2p spectra of the surface of HACl@Li electrode after being cycled for 0 h and 100 h. (f) *In situ* optical microscope images of the lithium deposition process on HACl@Li anode (upper) and pure Li anode (lower). Surface and cross-sectional morphology of HACl@Li electrode (g) and (h) and pure Li electrode (i) and (j) after being cycled for 100 h at current density of 1 mA cm^{-2} and capacity of 2 mA h cm^{-2}.

observed at the interface without HACl under altered electrode potential and concentration field (Fig. S33, ESI†). Galvanostatic polarization curve (Fig. 4(d)) evidences that the pure Li electrode shows very large space charge potential drop $\Delta\eta$ of about 66.8 mV. In contrast, negligible $\Delta\eta$ is observed in the HACl@Li electrode. The interfacial concentration field and electric field can be homogenized by immobilized TVI^- with high concentration at the HACl. Notably, Li electrode covered by LiTFSI/PEO layer, in which anions are not immobilized, still exhibits considerable SCL and $\Delta\eta$. This manifests that the PEO polymer chains only act as a flexible framework with great stability and desirable compatibility with lithium.

The stability of the interface is important for long-acting optimization of lithium deposition behavior. Because the HACl is a polymer interphase which is electrically insulated but ion-conductive, Li^+ will transfer through the interface and deposit beneath the HACl layer. Fig. S34 (ESI†) manifests that the HACl can remain at the surface of the lithium anode without exposed lithium, facilitating the stability of the HACl. Further, the long-term cyclic stability of HACl is also studied. The S 2p and N 1s spectra of HACl@Li electrode after being cycled for 100 h (Fig. 4(e) and Fig. S35, ESI†) show that common decomposition products of TVI^- such as S_n^{2-} (around 160.5 and 163.7 cm^{-1} in S 2p spectra) and LiN (around 397.5 cm^{-1} in N 1s spectra)[54] are not formed during cycling. This suggests that the HACl is long-acting to regulate lithium deposition without decomposition and exfoliation. The elemental mappings of HACl@Li electrode after cycling also manifest that the HACl can remain stable after repeated plating/stripping of lithium (Fig. S36, ESI†). Besides, the HACl electrode also maintains a low space charge overpotential after cycling for different times (Fig. S37, ESI†), indicating the long-term effectiveness of HACl. The C 1s and F 1s spectra of pure Li electrode and HACl@Li anode after cycling (Fig. S38, ESI†) also indicate that the HACl can obviously inhibit degradation of anions and solvents in the electrolyte. The immobilized TVI^- at the interface can reduce extra dissociative anions by electrostatic repulsion, thus preventing immoderate parasitic reaction.

Hence, the artificial HACl can effectively promote uniform deposition of lithium *via* desirable regulation of the interfacial

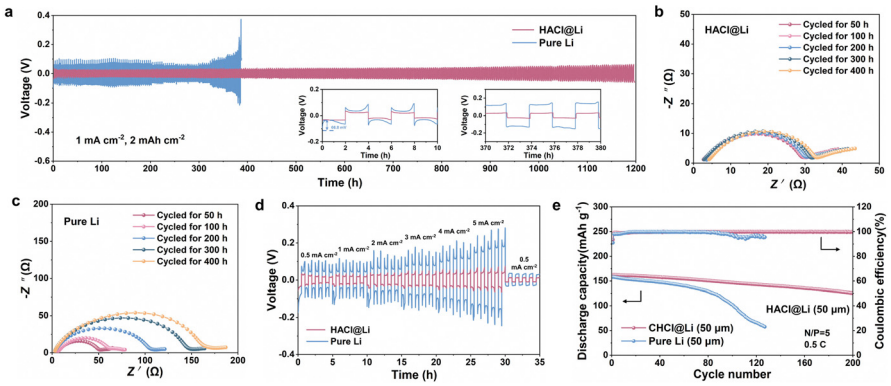

Fig. 5 (a) Cycling performance of Li||Li symmetric cells with HACl@Li electrode and pure Li electrode at a current density of 1 mA cm^{-2} and capacity of 2 mA h cm^{-2}. Electrochemical impedance spectra of Li||Li symmetric cells with HACl@Li electrode (b) and pure Li electrode (c) after being cycled for different times. (d) Rate performance of Li||Li symmetric cells with HACl@Li electrode and pure Li electrode at different current densities. (e) Cycling performance of full cells with NCM235 cathode with high load of active material (~2 mA h cm^{-2}) and limited lithium anode with/without HACl.

concentration field and electric field. *In situ* optical microscope observation shows that the HACl facilitates uniform and dense deposition of lithium, while the formation of SCL results in fast formation of Li dendrites (Fig. 4(f)). It also shows that the deposition of lithium will not lead to the formation of a new lithium layer and destruction of HACl, but to a gradual thickening of the modified lithium anode. Fig. 4(g), (h) and Fig. S39(a), (c) (ESI†) further display that the HACl@Li electrode exhibits uniform and compact deposition morphology and the cycled lithium layer is only 7.8 μm after being cycled for 100 h. In contrast, the pure Li electrode exhibits loose lithium deposition with abundant dendrites and massive "dead" lithium (52 μm in thickness) (Fig. 4(i), (j) and Fig. S39(b), (d), ESI†). The HACl can maintain a high anion concentration at the electrolyte/electrode interface to restrain the formation of SCL and inhibit parasitic reaction, thus facilitating uniform lithium deposition without dendrites during long-term cycling.

The cycling performance of Li||Li symmetric cells was further evaluated to verify the long-term cycling performance of the HACl@Li electrode. Fig. 5(a) shows that the HACl@Li electrode exhibits a stable cycling performance for over 1200 h with a low polarization voltage of less than 15 mV at a current density of 1 mA cm^{-2} and capacity of 2 mA h cm^{-2} in ester electrolyte. In contrast, the pure Li anode shows fast growth of polarization voltage and fluctuation after only 300 h. The long-term stability of the HACl@Li anode is superior to that of previously reported Li anodes protected by various artificial SEI layers (Table S3, ESI†). The variation of interfacial impedance after different cycles (Fig. 5(b)) also indicates that the HACl@Li electrode can maintain a low interfacial impedance of about 30 Ω after over 400 h, while the interfacial impedance of the pure Li electrode instantly increases to over 160 Ω after 400 h (Fig. 5(c)). The HACl exhibits superior interphase stability because it facilitates even multi-physics fields, uniform deposition of lithium and less parasitic reaction for the Li metal anode. The rate cycling performance of the HACl@Li anode (Fig. 5(d)) also manifests that the HACl can effectively mitigate the potential polarization caused by concentration gradient and SCL under high current density. The cycle performance under different current density and capacity was also investigated and the HACl@Li electrode also exhibits superior long-term cycling performance (Fig. S40 and S41, ESI†).

To further validate the compatibility and cyclic stability of HACl@Li, a full cell test with limited lithium was conducted. HACl-modified thin lithium foil (~50 μm) is matched with a high-load NCM523 cathode (~14 mg cm^{-2}). Fig. 5(e) and Fig. S42 (ESI†) show that the full cell with HACl@Li anode exhibits desirable cyclic performance, maintaining a discharge capacity retention of 77.6% (125.7 mA h g^{-1}) after 200 cycles at 0.5C. In contrast, the pure Li anode matched with NCM523 cathode exhibits a rapid polarization increase, severe voltage fluctuation, and decline of discharge capacity and CE after only 50 cycles. This can be ascribed to the exhaustion of active lithium and local short circuit caused by lithium dendrites. Due to the mitigation of SCL, the HACl can effectively promote the uniform plating/stripping of lithium and restrain parasitic reactions, thus enhancing the CE and long-term cycling performance. To further demonstrate the promising scale-up potential of the HACl layer, a pouch cell with HACl-modified thin lithium foil (~50 μm) matched with a high-load NCM523 cathode (~14 mg cm^{-2}) is assembled. Fig. S43 (ESI†) shows that the HACl@Li||NCM523 pouch cell demonstrated a high initial capacity of 147 mA h g^{-1} with a good capacity retention of 73% over 100 cycles at 1C.

Conclusions

The investigation of interfacial multi-physics fields is of great importance to the optimization of lithium deposition behavior. The ion concentration gradient and local electric field at the electrolyte/electrode interface will induce uncontrollable growth of lithium tips. In this work, the complicated multi-physics fields at the electrolyte/electrode interface are disclosed *via* a quantitative *in situ* Raman spectroscopy technique. It revealed the formation of an anion depletion layer at the

electrolyte/electrode interface during lithium deposition, generating SCL with local electric field and potential drop. The magnitude of SCL is highly related to the anions, solvation structure and solvent environment, and anion transport behavior is the core factor. Besides, the improvement of t_+ can availably mitigate the formation of SCL. Further, based on interface regulation, a high-anion-concentration interface *via* an anion immobilization strategy is proposed. The HACI can maintain a high concentration of anions at the electrolyte/electrode interface without affecting the ionic conductivity and viscosity of the bulk electrolyte. The HACI with immobilized anions can effectively suppress anion depletion at the interface and exhibits a high t_+ of 0.57, thus restraining the formation of SCL and local electric field. Besides, the HACI is a fast Li^+ transport interface which can rapidly supplement the consumption of Li^+ and ease concentration gradient of Li^+. As a result, the symmetrical cell with HACI@Li electrode exhibits a desirable cycling performance for over 1200 h with a with a low polarization voltage of 15 mV at a current density of 1 mA cm^{-2} and areal capacity of 2 mA h cm^{-2} in ester electrolyte. The full cell with high-load NCM523 cathode ($\sim$14 mg cm^{-2}) and limited HACI@Li anode ($\sim$50 μm) exhibits desirable cycling performance, maintaining a discharge capacity retention of 77.6% (125.7 mA h g^{-1}) after 200 cycles at 0.5C. This indicates that the optimization of multi-physics fields *via* interface architecture is an effective method to promote the uniform deposition of lithium and desirable long-term cycling performance. It provides us with a new perspective to regard the deposition behavior of lithium from interfacial multi-physics fields. The quantitative *in situ* Raman spectroscopy technique provides an effective method to clarify intricate interfacial processes, which can be further extended to various metal anodes and electrolyte systems, such as lithium anode, zinc anode, magnesium anode, high-concentration electrolyte, and electrolyte additives.

Author contributions

J. L., P. Z. and J. Z. conceived the idea. H. H. designed and synthesized related salts and polymers. J. L. designed and conducted *in situ* Raman measurements, material characterizations and electrochemical measurements. J. D. and J. Li helped design the *in situ* Raman measurement. H. H. performed the MD simulation. J. Lin performed the FEA modeling and calculations. Y. D. and N. P. helped with *in situ* Raman measurements, material characterizations. All authors discussed and analyzed the data. J. L., P. Z., J. D., J. Lin and J. Z. wrote and revised the paper.

Data availability

The authors confirm that the data supporting the findings of this study are available within the main text and ESI.†

Conflicts of interest

The authors declare that they have no known competing financial interests or personal relationships that could have appeared to influence the work reported in this paper.

Acknowledgements

The authors gratefully acknowledge financial support from the National Natural Science Foundation of China (grant no. 21875195, 21875198, 22005257, 21925404, 22222903 and 22021001), the Fundamental Research Funds for the Central Universities (20720190040), and the Industry-University-Research Joint Innovation Project of Fujian Province (2023H6029). The authors also would like to express gratitude for the support of Tan Kah Kee Innovation Laboratory.

Notes and references

1 B. Horstmann, J. Shi, R. Amine, M. Werres, X. He, H. Jia, F. Hausen, I. Cekic-Laskovic, S. Wiemers-Meyer, J. Lopez, D. Galvez-Aranda, F. Baakes, D. Bresser, C.-C. Su, Y. Xu, W. Xu, P. Jakes, R.-A. Eichel, E. Figgemeier, U. Krewer, J. M. Seminario, P. B. Balbuena, C. Wang, S. Passerini, Y. Shao-Horn, M. Winter, K. Amine, R. Kostecki and A. Latz, *Energy Environ. Sci.*, 2021, **14**, 5289–5314.
2 D. Deng, *Energy Sci. Eng.*, 2015, **3**, 385–418.
3 J. Liu, H. Ma, Z. Wen, H. Li, J. Yang, N. Pei, P. Zhang and J. Zhao, *J. Energy Chem.*, 2022, **64**, 354–363.
4 X.-B. Cheng, R. Zhang, C.-Z. Zhao and Q. Zhang, *Chem. Rev.*, 2017, **117**, 10403–10473.
5 X. R. Chen, B. C. Zhao, C. Yan and Q. Zhang, *Adv. Mater.*, 2021, **33**, e2004128.
6 X. Sun, X. Zhang, Q. Ma, X. Guan, W. Wang and J. Luo, *Angew. Chem., Int. Ed.*, 2020, **59**, 6665–6674.
7 X. B. Cheng, R. Zhang, C. Z. Zhao, F. Wei, J. G. Zhang and Q. Zhang, *Adv. Sci.*, 2016, **3**, 1500213.
8 H. Kwon, J.-H. Lee, Y. Roh, J. Baek, D. J. Shin, J. K. Yoon, H. J. Ha, J. Y. Kim and H.-T. Kim, *Nat. Commun.*, 2021, **12**, 5537.
9 Z. Huang, J.-C. Lai, S.-L. Liao, Z. Yu, Y. Chen, W. Yu, H. Gong, X. Gao, Y. Yang, J. Qin, Y. Cui and Z. Bao, *Nat. Energy*, 2023, **8**, 577–585.
10 Z. Sun, Y. Wang, S. Shen, X. Li, X. Hu, M. Hu, Y. Su, S. Ding and C. Xiao, *Angew. Chem., Int. Ed.*, 2023, e202309622.
11 L. Yue, X. Wang, L. Chen, D. Shen, Z. Shao, H. Wu, S. Xiao, W. Liang, Y. Yu and Y. Li, *Energy Environ. Sci.*, 2024, **17**, 1117–1131.
12 Q.-K. Zhang, X.-Q. Zhang, J. Wan, N. Yao, T.-L. Song, J. Xie, L.-P. Hou, M.-Y. Zhou, X. Chen, B.-Q. Li, R. Wen, H.-J. Peng, Q. Zhang and J.-Q. Huang, *Nat. Energy*, 2023, **8**, 725–735.
13 X.-B. Cheng, S.-J. Yang, Z. Liu, J.-X. Guo, F.-N. Jiang, F. Jiang, X. Xiong, W. Bo Tang, H. Yuan, J.-Q. Huang, Y. Wu and Q. Zhang, *Adv. Mater.*, 2023, 2307370.
14 S. Kim, J.-A. Lee, T. K. Lee, K. Baek, J. Kim, B. Kim, J. H. Byun, H.-W. Lee, S. J. Kang, J.-A. Choi, S.-Y. Lee,

M.-H. Choi, J.-H. Lee and N.-S. Choi, *Energy Environ. Sci.*, 2023, **16**, 5108–5122.
15 Y. Xia, P. Zhou, X. Kong, J. Tian, W. Zhang, S. Yan, W.-h Hou, H.-Y. Zhou, H. Dong, X. Chen, P. Wang, Z. Xu, L. Wan, B. Wang and K. Liu, *Nat. Energy*, 2023, **8**, 934–945.
16 M. S. Kim, Z. Zhang, P. E. Rudnicki, Z. Yu, J. Wang, H. Wang, S. T. Oyakhire, Y. Chen, S. C. Kim, W. Zhang, D. T. Boyle, X. Kong, R. Xu, Z. Huang, W. Huang, S. F. Bent, L.-W. Wang, J. Qin, Z. Bao and Y. Cui, *Nat. Mater.*, 2022, **21**, 445–454.
17 S. Li, J. Huang, Y. Cui, S. Liu, Z. Chen, W. Huang, C. Li, R. Liu, R. Fu and D. Wu, *Nat. Nanotechnol.*, 2022, **17**, 613–621.
18 J. Luo, Q. Huang, D. Shi, Y. Qiu, X. Zheng, S. Yang, B. Li, J. Weng, M. Wu, Z. Liu, Y. Yu and C. Yang, *Adv. Funct. Mater.*, 2024, 2403021.
19 K. Xu, *J. Power Sources*, 2023, **559**, 232652.
20 P. Zou, Y. Sui, H. Zhan, C. Wang, H. L. Xin, H. M. Cheng, F. Kang and C. Yang, *Chem. Rev.*, 2021, **121**, 5986–6056.
21 A. Jana and R. E. García, *Nano Energy*, 2017, **41**, 552–565.
22 X. Shen, R. Zhang, P. Shi, X. Chen and Q. Zhang, *Adv. Energy Mater.*, 2021, **11**, 2003416.
23 J. Wang, W. Huang, A. Pei, Y. Li, F. Shi, X. Yu and Y. Cui, *Nat. Energy*, 2019, **4**, 664–670.
24 H. J. S. Sand, *London, Edinburgh Dublin Philos. Mag. J. Sci.*, 1901, **1**, 45–79.
25 C. Brissot, M. Rosso, J. N. Chazalviel and S. Lascaud, *J. Power Sources*, 1999, **81–82**, 925–929.
26 M. Rosso, T. Gobron, C. Brissot, J. N. Chazalviel and S. Lascaud, *J. Power Sources*, 2001, **97–98**, 804–806.
27 V. Fleury, J. N. Chazalviel, M. Rosso and B. Sapoval, *J. Electroanal. Chem. Interfacial Electrochem.*, 1990, **290**, 249–255.
28 J. N. Chazalviel, *Phys. Rev. A: At., Mol., Opt. Phys.*, 1990, **42**, 7355–7367.
29 R. Cork, D. Pritchard and W. Y. Tam, *Phys. Rev. A: At., Mol., Opt. Phys.*, 1991, **44**, 6940–6943.
30 V. Fleury, J. Chazalviel and M. Rosso, *Phys. Rev. Lett.*, 1992, **68**, 2492–2495.
31 M. Rosso, J. N. Chazalviel, V. Fleury and E. Chassaing, *Electrochim. Acta*, 1994, **39**, 507–515.
32 V. Fleury, J.-N. Chazalviel, M. Rosso and B. Sapoval, *J. Electroanal. Chem. Interfacial Electrochem.*, 1990, **290**, 249–255.
33 V. Fleury, M. Rosso, J. N. Chazalviel and B. Sapoval, *Phys. Rev. A: At., Mol., Opt. Phys.*, 1991, **44**, 6693–6705.
34 H. Dai, J. Dong, M. Wu, Q. Hu, D. Wang, L. Zuin, N. Chen, C. Lai, G. Zhang and S. Sun, *Angew. Chem., Int. Ed.*, 2021, **60**, 19852–19859.
35 M. Kim, Y. Shin, K. Ahn, C. H. Lee and B. Kang, *J. Power Sources*, 2022, **532**, 231348.
36 A. Pei, G. Zheng, F. Shi, Y. Li and Y. Cui, *Nano Lett.*, 2017, **17**, 1132–1139.
37 K. Yan, Z. Lu, H.-W. Lee, F. Xiong, P.-C. Hsu, Y. Li, J. Zhao, S. Chu and Y. Cui, *Nat. Energy*, 2016, **1**, 16010.
38 Y. Okajima, Y. Shibuta and T. Suzuki, *Comput. Mater. Sci.*, 2010, **50**, 118–124.
39 G. Yang, I. N. Ivanov, R. E. Ruther, R. L. Sacci, V. Subjakova, D. T. Hallinan and J. Nanda, *ACS Nano*, 2018, **12**, 10159–10170.
40 Y. Gu, E.-M. You, J.-D. Lin, J.-H. Wang, S.-H. Luo, R.-Y. Zhou, C.-J. Zhang, J.-L. Yao, H.-Y. Li, G. Li, W.-W. Wang, Y. Qiao, J.-W. Yan, D.-Y. Wu, G.-K. Liu, L. Zhang, J.-F. Li, R. Xu, Z.-Q. Tian, Y. Cui and B.-W. Mao, *Nat. Commun.*, 2023, **14**, 3536.
41 Y.-H. Wang, S. Zheng, W.-M. Yang, R.-Y. Zhou, Q.-F. He, P. Radjenovic, J.-C. Dong, S. Li, J. Zheng, Z.-L. Yang, G. Attard, F. Pan, Z.-Q. Tian and J.-F. Li, *Nature*, 2021, **600**, 81–85.
42 J. Zhao, M. Cano, J. J. Giner-Casares, R. Luque and G. Xu, *Energy Environ. Sci.*, 2020, **13**, 2618–2656.
43 S. Hwang, D.-H. Kim, J. H. Shin, J. E. Jang, K. H. Ahn, C. Lee and H. Lee, *J. Phys. Chem. C*, 2018, **122**, 19438–19446.
44 Z. Wei, A. Salehi, G. Lin, J. Hu, X. Jin, E. Agar and F. Liu, *J. Power Sources*, 2020, **449**, 227361.
45 X. Ren, L. Zou, X. Cao, M. H. Engelhard, W. Liu, S. D. Burton, H. Lee, C. Niu, B. E. Matthews, Z. Zhu, C. Wang, B. W. Arey, J. Xiao, J. Liu, J.-G. Zhang and W. Xu, *Joule*, 2019, **3**, 1662–1676.
46 S. C. Kim, J. Wang, R. Xu, P. Zhang, Y. Chen, Z. Huang, Y. Yang, Z. Yu, S. T. Oyakhire, W. Zhang, L. C. Greenburg, M. S. Kim, D. T. Boyle, P. Sayavong, Y. Ye, J. Qin, Z. Bao and Y. Cui, *Nat. Energy*, 2023, **8**, 814–826.
47 J. Li, H. Hua, X. Deng, P. Lai, Y. Kang, S. Kuang, F. Wang, X. Zeng, Y. Zhang and J. Zhao, *Chem. Eng. J.*, 2023, **452**, 139398.
48 G. A. Giffin, *Nat. Commun.*, 2022, **13**, 5250.
49 P. Lai, B. Huang, X. Deng, J. Li, H. Hua, P. Zhang and J. Zhao, *Chem. Eng. J.*, 2023, **461**, 141904.
50 X. Peng, T. Wang, B. Liu, Y. Li and T. Zhao, *Energy Environ. Sci.*, 2022, **15**, 5350–5361.
51 X. Cao, L. Zou, B. E. Matthews, L. Zhang, X. He, X. Ren, M. H. Engelhard, S. D. Burton, P. Z. El-Khoury, H.-S. Lim, C. Niu, H. Lee, C. Wang, B. W. Arey, C. Wang, J. Xiao, J. Liu, W. Xu and J.-G. Zhang, *Energy Storage Mater.*, 2021, **34**, 76–84.
52 D. Ensling, M. Stjerndahl, A. Nytén, T. Gustafsson and J. O. Thomas, *J. Mater. Chem.*, 2009, **19**, 82–88.
53 T. Naren, G.-C. Kuang, R. Jiang, P. Qing, H. Yang, J. Lin, Y. Chen, W. Wei, X. Ji and L. Chen, *Angew. Chem., Int. Ed.*, 2023, **62**, e202305287.
54 C. Xu, B. Sun, T. Gustafsson, K. Edström, D. Brandell and M. Hahlin, *J. Mater. Chem. A*, 2014, **2**, 7256–7264.

